Nanoscale

PAPER

View Article Online
View Journal | View Issue

Open Access Article. Published on 24 November 2016. Downloaded on 7/24/2025 7:54:59 PM.
This article is licensed under a Creative Commons Attribution-NonCommercial 3.0 Unported Licence.

Cite this: *Nanoscale*, 2017, **9**, 621

Two-dimensional hexagonal CrN with promising magnetic and optical properties: A theoretical prediction†

Artem V. Kuklin,[a,b] Alexander A. Kuzubov,*[a,c] Evgenia A. Kovaleva,[a] Natalya S. Mikhaleva,[a] Felix N. Tomilin,[a,c] Hyosun Lee[b] and Pavel V. Avramov[b]

Received 4th October 2016,
Accepted 23rd November 2016

DOI: 10.1039/c6nr07790k

www.rsc.org/nanoscale

Half-metallic ferromagnetic materials with planar forms are promising for spintronics applications. A wide range of 2D lattices like graphene, *h*-BN, transition metal dichalcogenides, *etc*. are non-magnetic or weakly magnetic. Using first principles calculations, the existence of graphene-like hexagonal chromium nitride (*h*-CrN) with an almost flat atomically thin structure is predicted. We find that freestanding *h*-CrN has a 100% spin-polarized half-metallic nature with possible ferromagnetic ordering and a high rate of optical transparency. As a possible method for stabilization and synthesis, deposition of *h*-CrN on 2D $MoSe_2$ or on MoS_2 is proposed. The formation of composites retains the half-metallic properties and leads to the reduction of spin-down band gaps to 1.43 and 1.71 eV for energetically favorable *h*-CrN/$MoSe_2$ and *h*-CrN/MoS_2 configurations, respectively. Calculation of the dielectric functions of *h*-CrN, *h*-CrN/$MoSe_2$ and *h*-CrN/MoS_2 exhibit the high transparency of all three low-dimensional nanomaterials. The honeycomb CrN may be considered as a promising fundamental 2D material for a variety of potential applications of critical importance.

Introduction

Since the discovery of graphene, two-dimensional (2D) materials have attracted much attention due to their unique physical properties, which are very different from their bulk crystal analogs. For example, graphene – one atomic thick hexagonal layer of carbon – displays excellent thermal and electronic conductivity and reveals a unique Dirac cone in its electronic structure.[1,2] In recent years many novel materials that were originally considered to exist only in the framework of theory have been synthesized. They include graphene analogues such as silicene,[3,4] germanene,[5] phosphorene,[6] and even un-layered stanene[7] and one-atom-thick boron (borophene).[8]

During the last decade, researchers have discovered a number of different methods for the synthesis and manipulation of low-dimensional materials[9] providing new two-dimensional (2D) structures to be obtained and allowing their properties to be managed through the creation of defects, modification by adatoms and integration into composites for a wide range of applications. Nanoelectronics, and in particular spintronics, are probably the most important applications of two-dimensional materials.

In the last few years, two-dimensional magnetism has attracted much attention due to the possibility of the formation of magnetic and spintronic devices using two-dimensional layers.[10–12] It was recently reported that oxidized few-layer black phosphorous nanomeshes have a three-order-larger edge ferromagnetism than of graphene nanomeshes.[13] However, most 2D lattices like graphene, *h*-BN, transition metal dichalcogenides, *etc*. are non-magnetic or weakly magnetic. For this reason, various ferromagnetic substrates have been used for spin injection to induce spin polarization of low-dimensional non-magnetic fragments for spin-related applications.[14–16] Thin films of transition metal nitrides (TMNs) may provide one more possibility to obtain low-dimensional materials with unique spin-related properties because unpaired d-electrons are responsible for the formation of spin-ordered surface electronic states. Chromium nitride is a typical example of the TMNs family. Its bulk phase has a

[a]*Siberian Federal University, 79 Svobodny pr., Krasnoyarsk 660041, Russia. E-mail: alexxkuzubov@gmail.com*
[b]*Department of Chemistry, Kyungpook National University, 80 Daehakro, Bukgu, Daegu 41566, Republic of Korea*
[c]*L.V. Kirensky Institute of Physics, 50/38 Akademgorodok, Krasnoyarsk 660036, Russia*

† Electronic supplementary information (ESI) available: The GGA DFT optimized geometry for the bulk CrN, $MoSe_2$ and MoS_2; phonon band structure; equilibrium structure of the *h*-CrN nanocluster; equi-biaxial strain *vs*. energy and *vs*. stress plot for *h*-CrN; isosurface of *h*-CrN AFM state; band structures and densities of states of both composites; spatial charge distribution of *h*-CrN, *h*-CrN/$MoSe_2$, *h*-CrN/MoS_2. See DOI: 10.1039/c6nr07790k

Open Access Article. Published on 24 November 2016. Downloaded on 7/24/2025 7:54:59 PM.
This article is licensed under a Creative Commons Attribution-NonCommercial 3.0 Unported Licence.

simple NaCl-type structure with $Fm\bar{3}m$ symmetry (paramagnetic under normal conditions) and an orthogonal phase with *Pnma* symmetry (antiferromagnetic).[17,18] Miao and Lambrecht have discovered that the cubic phase is energetically more stable.[19] It undergoes the first-order phase transition from the paramagnetic to the antiferromagnetic state with layered ordering of the magnetic moments when the temperature drops below 273 K.[20–22] This means that every individual layer is a ferromagnet. Therefore, ferromagnetic ordering can be expected in 2D lattices of CrN. The substrates based on MgO, Pt or Al_2O_3 are generally used to obtain TMNs films.[23–26] CrN thin films possess a different Néel temperature and have a slight distortion in the (001) orientation, whereas the structural distortion of the CrN (111) film is not observed.[23]

Recently, monolayers of TM carbides and nitrides are actively investigated due to their potential wide application in lithium-ion batteries,[27–29] electrocatalysts of hydrogen decomposition[30] and nanoelectronics.[31–37] Practice preparation of two-dimensional titanium carbides with OH-terminated surface demonstrated that some transition metal carbides (including mixed carbides) can also be synthesized by dipping into hydrogen fluoride acid followed by sonication.[38] Subsequently two-dimensional vanadium (V_2C) and niobium (Nb_2C) carbides were synthesized.[39] The structures of TM nitrides in most cases are similar to TM carbides due to the similar bonding type.[40] Using electronic structure calculations, it was found that the one-atom-thick CrN (100) layer demonstrates spontaneous half-metallic ferromagnetism.[34] The magnetic properties of the VN (111) monolayer and its composite with MgO (111) were studied using a DFT approach and DOS analysis.[36] It was shown that the VN monolayer is spin-polarized and retains its properties after contact with the MgO substrate. In ref. 41, the slab thicknesses for spontaneous conversion from cubic to layered graphitic structures were determined for a number of crystalline lattices. The layered honeycomb structures are more favorable than the cubic ones for ultrathin films, including diamond, boron nitride, silicon carbide, boron phosphide and rock salt. Recently photocatalytic and piezoelectric properties with spontaneous polarization were demonstrated in the tetragonal and hexagonal forms of the NbN rocksalt structure.[42] Monolayers of some transition-metal carbides MC (M = Zr, Hf) demonstrate a quantum spin Hall effect at the nanoscale.[43] A short literature survey of both experimental and theoretical publications reveals a very promising possibility to develop honeycomb TMN monolayers with unique electronic and magnetic properties that provide a new perspective for spintronic applications.

In this work, the results of density functional theory (DFT+U) with consideration of weak dispersion interactions indicate directly the possibility to create a 2D chromium nitride monolayer of (111) crystallographic orientation being a 100% spin-polarized half-metallic material with high degree of optical transparency. The electronic structure calculations reveal the good match of the *h*-CrN crystalline lattice with 2D MoS_2 and $MoSe_2$ substrates, which opens a unique way for experimental synthesis and stabilization of 2D CrN. The results can be used for the prediction of new stable 2D polymorphs of TMNs and discovering new properties at the nanoscale.

Computational methods

All atomic and electronic structure calculations were performed using density functional theory (DFT)[44,45] in the generalized gradient approximation with the Hubbard correction (GGA+U),[46,47] as implemented in the Vienna *Ab initio* Simulation Package (VASP).[48,49] The projector augmented wave (PAW)[50] method and Perdew–Burke–Ernzerhof (PBE)[51] exchange functional were employed. The parameter $U^* = U - J$ equal to 3 eV was chosen based on the previous studies of chromium nitride to take into account strong electron correlations.[34,52] D3 Grimme correction of weak dispersion interactions[53] and the Periodic Boundary Conditions (PBC) approach were used to perform electronic structure calculations of all 2D structures. To evaluate the relevance of these results, the long-corrected hybrid functional proposed by Heyd, Scuseria, and Ernzerhof (HSE06) was employed.[54] The plane-wave energy cutoff was set to 500 eV. A vacuum region of 15 Å was set to avoid artificial interaction between neighboring images. The reciprocal space in the Brillouin zone was sampled using the Monkhorst–Pack scheme[55] with 15 × 15 × 1 and 21 × 21 × 1 *k*-points for the monolayer and composites, respectively. The convergence tolerances for the force and electronic minimizations were 0.001 eV $Å^{-1}$ and 10^{-6} eV, respectively. The phonon frequency calculations were carried out in a supercell (4 × 4 × 1) using the density functional perturbation theory (DFPT)[56] and the PHONOPY code.[57]

Results and discussion

To design the initial structural model of the two-dimensional one-atom thick CrN (111) film, an equilibrium geometry of the rocksalt-structured unit cell of CrN was optimized using the electronic structure calculations (see ESI†). Fig. 1 illustrates the schematic representation of the hexagonal 2D CrN (*h*-CrN)

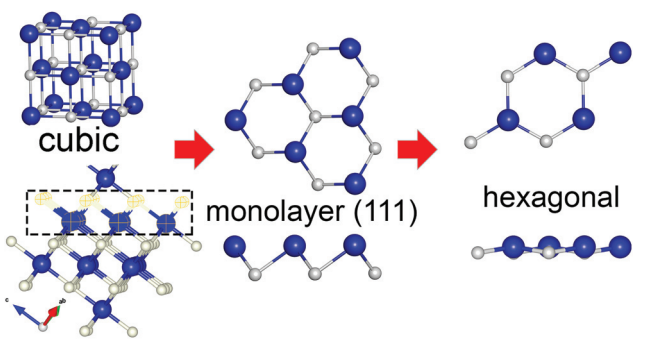

Fig. 1 Schematic representation of *h*-CrN formation. Blue and grey balls correspond to Cr and N atoms, respectively.

This journal is © The Royal Society of Chemistry 2017

Open Access Article. Published on 24 November 2016. Downloaded on 7/24/2025 7:54:59 PM.
This article is licensed under a Creative Commons Attribution-NonCommercial 3.0 Unported Licence.

formation and its atomic structure. The unit is simple in structure and can be described as a monolayer of respective surface. The energy minimization of the corrugated (111)-oriented CrN monolayer resulted in the formation of an almost flat hexagonal sheet with minor buckling due to the reduction of a surface dipole moment. The value of buckling is ±0.071 Å (from the perfect plane) along the vacuum direction for both Cr and N atoms. The optimized *h*-CrN unit cell contains one chromium and one nitrogen atom with a Cr–N bond length equal to 1.884 Å, which is noticeably shorter than in the bulk (2.11 Å). Formation of *h*-CrN leads to the elongation of the translation vector from 2.989 Å of the exfoliated CrN (111) monolayer up to 3.258 Å of the hexagonal 2D structure. The CrN monolayer of the (110) surface also considered. During atomic force relaxations one transforms into a CrN (100) monolayer, which is discussed in ref. 33. To check the possibility of global minimum finding, we created a perfectly flat structure of CrN (111) which is an analog of graphene or *h*-BN. It was found that the fully relaxed structure of the flat CrN sheet is 0.01 eV higher in energy.

The stability of low-dimensional (1D and 2D) systems has been of key interest since the foundation of quantum and statistical mechanics.[58,59] The dynamic stability of the *h*-CrN sheet is confirmed from the phonon frequency calculations. The calculated phonon dispersion (Fig. S1†) contains a very small imaginary acoustic frequency of 0.25 cm^{-1}, which could be caused by phonon–magnetic coupling or strong electron correlations. Such a small value can be ignored and thus the structure can be considered as dynamically stable.[60,61] Similar to the phonon frequency of graphene,[62] there are three distinct acoustic modes in the phonon spectra of *h*-CrN, which are caused by the acoustic summation rule insufficiency. In the lattice dynamics calculations based on DFPT there is a persistent problem of non-vanishing frequencies of acoustic modes.[63]

Sometimes, due to the breakdown of translational symmetry for low-dimensional materials with non-equivalent sublattices, phonon calculations in periodic boundary conditions cannot be used to prove whether or not a low-dimensional crystalline lattice is a local or global minimum.[64] The force constants also can be affected by phonon–magnetic coupling or strong electron correlations and soft modes may take place in magnetic and/or correlated low-dimensional systems.[65,66] The newly proposed *h*-CrN is an example of a strongly correlated low-dimensional magnetic material with non-equivalent sublattices. Since the phonon dispersion calculations in periodic boundary conditions may not provide the final proof of *h*-CrN structural stability due to the presence of nonequivalent sublattices, strong correlation effects and phonon–magnetic coupling, the electronic structure calculations of extended finite nanocluster consisted of 48 atoms performed at the Γ-point (1 × 1 × 1 *k*-point mesh). To avoid artificial interactions between the cluster images, the vacuum interval of 20.8 Å and 9.6 Å along the perpendicular and planar directions were used. As the result of force minimization, the nanocluster becomes flat and retains in general its original crystalline lattice (see Fig. S2†) with small distortions at the edge atoms due to the edge effects. Therefore, no uncompensated mechanical stress takes place in the nanocluster and *h*-CrN can be considered as stable.

The structural stability under strain is very important for *h*-CrN synthesis and further applications. The *h*-CrN sheet is investigated by applying an equi-biaxial tensile strain (Fig. S3†) in accordance with formula (1) to estimate the mechanical stability and properties under strain.

$$\text{Strain}, \% = \frac{a_1 - a}{a} \times 100\% \quad (1)$$

where a and a_1 are lattice parameters before and after strain.

Fig. S3† shows that maximum stress occurs at 16%. Therefore, the elastic limit of the *h*-CrN sheet is at 0.16 strain with a maximum stress of 6.51 GPa. The supercell approach using 3 × 3 unit cells gives perfectly the same results in terms of energy and a very close result in terms of stress (Δ = 0.01 MPa). Therefore, no extra periodicity is found for the *h*-CrN nanosheet.

To evaluate the magnitude of exchange interactions and to find whether the ferromagnetic (FM) state is energetically favorable, the total energy spin-polarized calculations of ferromagnetic and antiferromagnetic (AFM) states of 2D *h*-CrN were performed using the 2 × 2 supercell. At the PBE level of theory, the ferromagnetic state is 0.715 eV lower in energy than the AFM configuration (Fig. S4†). Fig. 2(a) shows the spin density distribution of the FM configuration. Most of the spin-up density is localized on Cr^{2+} ions with a small portion of minority spin density localized on the nitrogen ions. The Bader analysis[67] revealed an electron charge transfer of 1.52*e* from the transition metal to nitrogen. It is found that the charge density (Fig. 2(b)) is mainly distributed over N atoms and, in particularly, along three Cr–N bonds making in-plane orbitals responsible for the bond formation. To understand the bonding characteristics, the electron localization function (ELF)[68,69] is calculated and plotted in Fig. 2(c). The ELF map is presented in values between 0.0 and 1.0. The value of 1.0 corresponds to the total of localized electrons. The electrons are localized at N atoms in the plane of the sheet, indicating that the atomic orbitals of nitrogen are characterized by sp^2 hybridization. The electron density responsible for the formation of bonds is shifted towards nitrogen atoms. The N p_z-orbitals correspond to the green part of ELF, revealing delocalized features. The blue distribution localized around Cr atoms indicates the electron deficiency of Cr atoms, which is in good agreement with the Bader charge analysis.

At the PBE level of theory, the total and partial densities of states and spin-separated band structure of *h*-CrN are presented in Fig. 2(d) and (e). The top spin-up valence band touches the Fermi level in the Γ–M and K–Γ intervals and the bottom of the *h*-CrN conductivity band crosses the Fermi level in the vicinity of the K-point. The minimum of the conductivity band is localized exactly at the K-point of the Brillouin zone with an energy of −0.2 eV. Partial filling of the spin-up conduction band provides a non-zero density of states at the

Open Access Article. Published on 24 November 2016. Downloaded on 7/24/2025 7:54:59 PM.
This article is licensed under a Creative Commons Attribution-NonCommercial 3.0 Unported Licence.

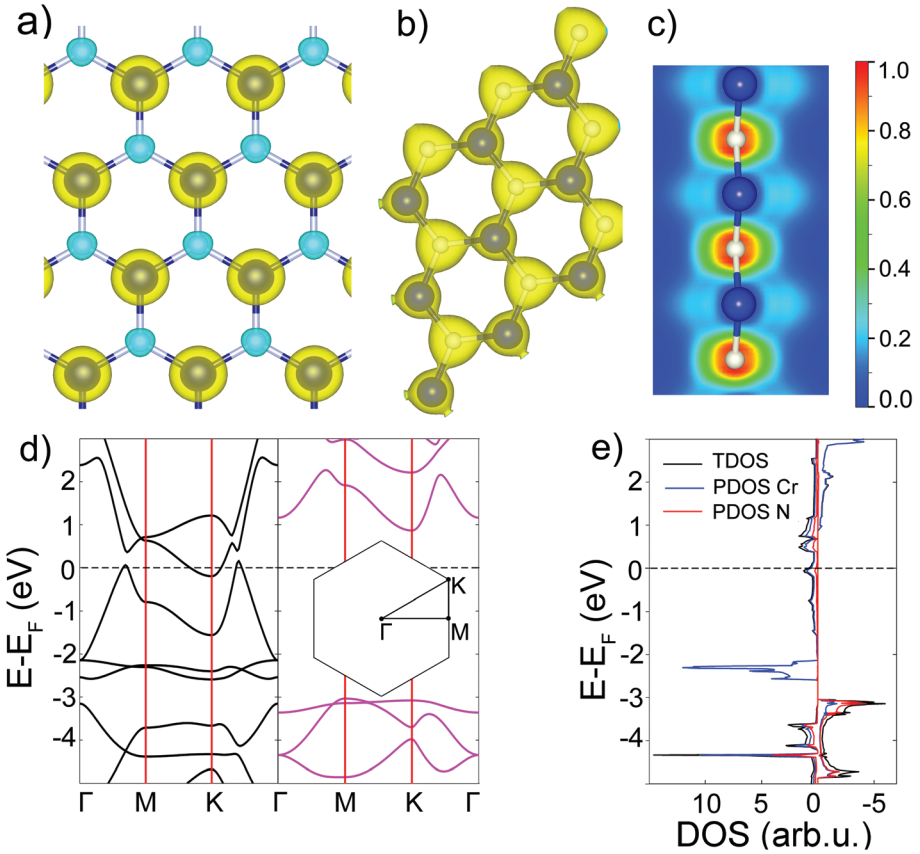

Fig. 2 The electronic structure of *h*-CrN. (a) Isosurface (0.04 e Å^{-3}) of spatial spin density distribution. The blue and green spheres correspond to majority and minority spin density, respectively. (b) Isosurface (0.1 e Å^{-3}) of the total electronic charge density. (c) ELF map renormalized to values between 0.0 and 1.0. (d) Spin-separated band structures. Spin-up and spin-down are presented in black and pink, respectively. (e) Total and partial densities of states. TDOS, Cr PDOS and N PDOS are in black, blue and red, respectively.

Fermi level which, in combination with the spin-down band gap of 3.9 eV width, results in the 100% spin-polarized half-metallic properties of *h*-CrN.

Spin polarization at the Fermi level is calculated as:

$$\xi = \frac{n_\uparrow - n_\downarrow}{n_\uparrow + n_\downarrow}, \quad (2)$$

where $n_\uparrow$ and $n_\downarrow$ are the spin-up and spin-down electron densities at the Fermi level, respectively. The work constitutes the first report of freestanding one-atom thick inorganic analogues of graphene with half-metallic properties.

The HSE06 hybrid functional is used to compare the result with a higher level of theory and evaluate corrections to the spin-down band gap, which is important in optical properties evidence. In 2D systems the results of HSE06 bandgaps sometimes can be compared to the quasi-particle GW bandgaps due to the cancelling of the neglecting excitons effect.[70,71] The results of HSE06 calculations demonstrate perfectly the same band gap of spin-down (3.9 eV). Bader analysis based on both PBE and HSE06 spin densities, revealing the same $3\mu_B$ total magnetic moment on the Cr^{2+} ions, which is comparable with experimental data ($3.17\mu_B$ (ref. 21)) for crystalline CrN.

Cr d-, Cr p-, Cr s-, N p-, N s-orbital-projected atomic densities of states and spatial distributions of spin density in certain energy regions of the *h*-CrN sheet are presented in Fig. 3(a) and (b), respectively. The distribution of peaks exhibits separation of the nitrogen valence orbitals into two groups: N sp_xp_y (a set of peaks in the [−5.73: −3.60] and [−4.85: −3.00] eV energy regions for spin-up and spin-down states, respectively); and N p_z (a single peak localized in the [−4.44: −4.31] and [−3.36: −3.07] eV energy regions for spin-up and spin-down channels, respectively). Such separation of the peaks suggests sp^2 hybridization of nitrogen ions. At the same time, partial peaks of Cr s, d_{xy} and $d_{x^2-y^2}$ states are localized in the same energy range as N s, p_x and p_y hybrid orbitals and demonstrate the exact same electronic resonance, revealing a strong overlap between them and the formation of sigma bonds lying in the *h*-CrN plane. Since the intensity of Cr p PDOSes is very low (in Fig. 3(a) all Cr p PDOSes are multiplied by 5 or 10), the involvement of p-orbitals in bond formation and therefore hybridization processes is minor. Spatial distribution of electronic density (Fig. 3(b)) in the range [−5.73: −5.55] eV unambiguously demonstrates the formation of σ-type Cr–N bonds caused by overlap of Cr sd^2 and N sp^2 hybrid orbitals.

This journal is © The Royal Society of Chemistry 2017

Open Access Article. Published on 24 November 2016. Downloaded on 7/24/2025 7:54:59 PM.
This article is licensed under a Creative Commons Attribution-NonCommercial 3.0 Unported Licence.

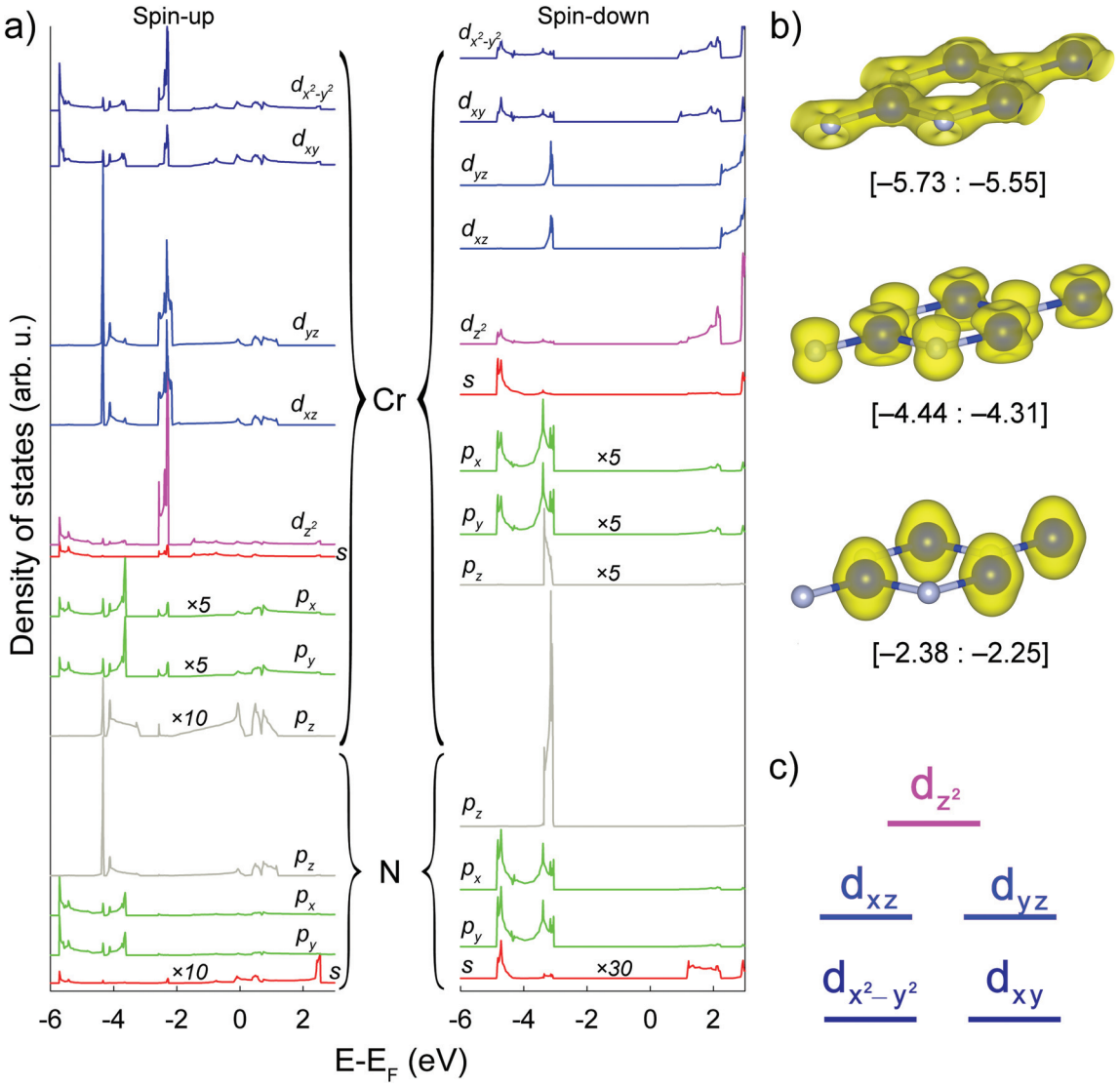

Fig. 3 (a) Orbital-projected atomic densities of states of the *h*-CrN sheet. From top to bottom in braces: Cr and N orbitals, respectively. Spin-up and spin-down channels are from left to right. The densities of Cr p and N s-orbitals are multiplied by appropriate values 5, 10 or 30, respectively. The Femi level is set to zero. (b) Spatial charge distribution in [−5.73; −5.55], [−4.44; −4.31], [−2.38; −2.25] eV energy regions. (c) Qualitative Cr d-orbital diagram of *h*-CrN.

Cr d_{xz} and d_{yz}-orbitals form another group of peaks distributed in the energy range of [−4.44: −4.31] eV (Fig. 3(a)) overlapping with p_z-orbitals in the same energy region, resulting in p–d overlap with the formation of π-dative bonds delocalized out-of-the-plane of Cr_3N_3 hexagons (Fig. 3(b)). The energy region of [−2.38: −2.25] eV (Fig. 3(b)) is characterized by chromium non-binding electronic levels where the states are localized only on the Cr ions keeping N ions naked. The electronic states are constituted by all types of Cr d-orbitals, with the main contribution from the Cr d_{z^2}-orbital.

The Cr d-orbital diagram of *h*-CrN is presented in Fig. 3(c). The non-degenerate non-bonding Cr d_{z^2}-orbital has the highest energy and is localized on the top of valence band (energy range [−2.38: −2.25] eV). The next in energy ([−4.44: −4.31] eV) are the double-degenerate Cr d_{xz} and Cr d_{yz} orbitals which overlap with N p_z states and form bonding π-dative orbitals localized above and below the sheet. The lowest in energy ([−5.73; −5.55] eV) doubly degenerate Cr d_{xy} and Cr $d_{x^2-y^2}$ states hybridize with Cr s-orbitals forming three Cr sd^2 hybrid states. These orbitals overlap with N sp^2 hybrid states and form σ-type bonding which forms the hexagonal sheet. The Cr d-orbital diagram of *h*-CrN is a typical example of the crystalline orbitals of trigonal-type complexes in terms of crystal field theory.

In practice, a synthesis of thin films is performed on substrates, which in many cases may stabilize the structure as well as affect the main structural features and properties of films. Growth of the two-dimensional CrN sheet on the appropriate substrate can be provided by CVD or PVD methods. The symmetry and lattice parameters of $MoSe_2$ and MoS_2 almost

Open Access Article. Published on 24 November 2016. Downloaded on 7/24/2025 7:54:59 PM.
This article is licensed under a Creative Commons Attribution-NonCommercial 3.0 Unported Licence.

perfectly match the structural parameters of *h*-CrN with minor differences in the lateral translation vector of about 1–2.8% (see ESI†) and can be regarded as perfect substrates for *h*-CrN synthesis. We propose that this is a relevant value to grow a structure. For example, graphene can be grown on different substrates like Ni, Cu, Pt *etc*. that have different lattice parameters.[72,73] Despite the fact that the mismatch between SiC (3.073 Å) and graphene (2.46 Å) is very large, the growth of graphene on SiC has been successfully produced.[74] In addition, $MoSe_2$ and MoS_2 are nonpolar materials. Their surfaces are rather chemically inert and can easily adopt 2D modification, which is extremely important for use in nanoelectronics.

Based on the equilibrium geometry of $MoSe_2$ and MoS_2 monolayers (see ESI†), the *h*-CrN/$MoSe_2$ and *h*-CrN/MoS_2 bilayered heterostructures were simulated using the 21 × 21 *k*-point mesh along the periodical directions. Since the lattices of dichalcogenides have a minor mismatch with *h*-CrN, single unit cells were adapted to DFT+U PBE calculations. Only the most probable mutual configurations of *h*-CrN on $MoSe_2$(MoS_2) monolayers were considered, specifically with Cr ions coordinated either atop S(Se) ions or hollow sites, and N ions were coordinated atop Mo ions or hollow sites. The least favorable configurations, with transition metal ions (Mo and Cr) located above each other, as well as N arranged over Se(S) were not considered due to having the same sign of atomic charges of the partners.

Three possible configurations of *h*-CrN/$MoSe_2$ and *h*-CrN/MoS_2 heterostructures were revealed (Fig. 4), namely: (a) Cr_[S]–N_[Mo] or Cr_[S]–N_[Mo]; (b) Cr_[Se]–N_[hex] or Cr_[S]–N_[hex]; (c) Cr_[hex]–N_[Mo]. Here the coordination partners of *h*-CrN atoms (either Cr or N) are presented in square brackets and the coordination pairs are separated by dashes. The symbol [hex] denotes the location of the Cr or N ions above the centers of either $MoSe_2$ or MoS_2 hexagons.

The cohesive energies of the composites (CrN/MoS_2 and CrN/$MoSe_2$) were evaluated according to the following formula:

$$E_C = E_T - E_T\,[\mathrm{CrN}] - E_T\,[\mathrm{sub}] \quad (3)$$

where E_T is the total energy of either *h*-CrN/$MoSe_2$ or *h*-CrN/MoS_2 composites; E_T [CrN] is the energy of freestanding 2D CrN and E_T [sub] is the energy of the $MoSe_2$ or MoS_2 substrates.

The lowest-energy configuration of *h*-CrN/$MoSe_2$, with a cohesive energy of −0.402 eV, is Cr_[Se]–N_[Mo]. However, the Cr_[Se]–N_[hex] configuration is only 0.004 eV higher in energy (E_C = −0.398 eV). The energy difference (0.053 eV) between the lowest and the highest in energy configurations (Cr_[hex]–N_[Mo], E_C = −0.349 eV) is also considerably low. Since all localized configurations have only minor differences in energy, all three types of interfaces may be discovered experimentally. For the *h*-CrN/MoS_2 heterostructure, the same Cr_[S]–N_[Mo] and Cr_[S]–N_[hex] configurations with very close cohesive energies of −0.485 eV and −0.483 eV, respectively, were localized. The energy difference (0.002 eV) between

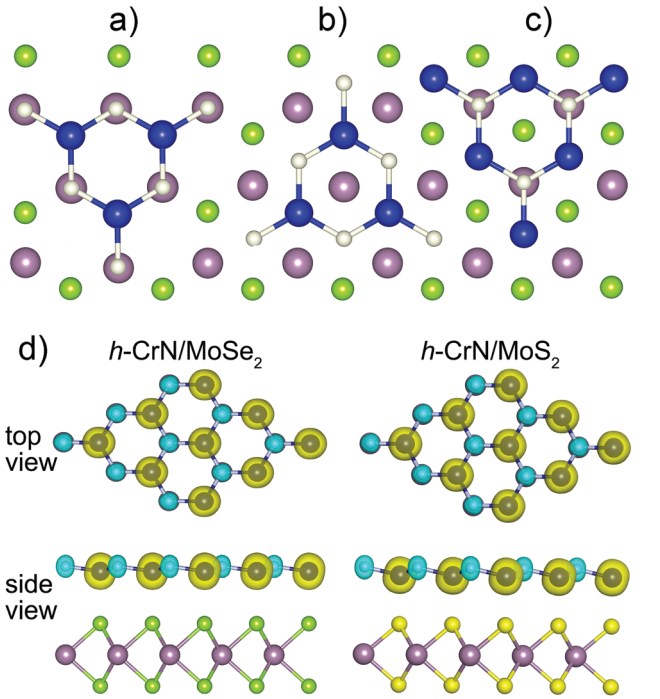

Fig. 4 Configurations of both *h*-CrN/$MoSe_2$ and *h*-CrN/MoS_2 heterostructures. (a) Cr_[Se]–N_[Mo] and Cr_[S]–N_[Mo]. (b) Cr_[Se]–N_[hex] and Cr_[S]–N_[hex]. (c) Cr_[hex]–N_[Mo]. Blue, beige, green-yellow and light purple balls correspond to Cr, N, Se (or S) and Mo atoms, respectively. (d) Equilibrium geometries and spatial spin density distributions of *h*-CrN/$MoSe_2$ and *h*-CrN/MoS_2 composites (isosurface level is 0.03 e Å^{-3}) in the lowest in energy configuration. The blue and green spheres correspond to the minority and majority spin densities.

configurations is minor, so either the first or the second configuration cannot be assigned as the energetically preferable one. The cohesive energy of the third Cr_[hex]–N_[Mo] configuration is 0.114 eV higher the lowest one.

The cohesive energies and interplanar distances reveal the weak binding between the *h*-CrN and $MoSe_2$(MoS_2) fragments with 2.812 Å and 2.514 Å measured as Cr–Se and Cr–S distances. Short interlayer distances between *h*-CrN and dichalcogenides sheets can be explained by the orbital overlap, which will be presented in a later section and electrostatic interactions between positive (Cr and Mo atoms) and negative (N and Se or S) atomic charges of the fragments. The stronger binding in *h*-CrN/MoS_2 composites is caused by the higher electronegativity and smaller atomic radius of sulfur ions. All configurations have their equilibrium geometry characterized by the location of nitrogen atoms slightly above the plane of *h*-CrN (Fig. 4(d)).

Despite the fact that energy difference between configurations is minor, different positions of atoms may affect the electronic structure of the whole composite. To find this out, band structures and spin-polarized DOSes of *h*-CrN/$MoSe_2$ and *h*-CrN/MoS_2 heterostructures (Fig. 5, S5 and S6†) were calculated. The interactions of *h*-CrN and $MoSe_2$ lead to the spin-polarization of the $MoSe_2$ fragment and cause the formation of

This journal is © The Royal Society of Chemistry 2017

Open Access Article. Published on 24 November 2016. Downloaded on 7/24/2025 7:54:59 PM.
This article is licensed under a Creative Commons Attribution-NonCommercial 3.0 Unported Licence.

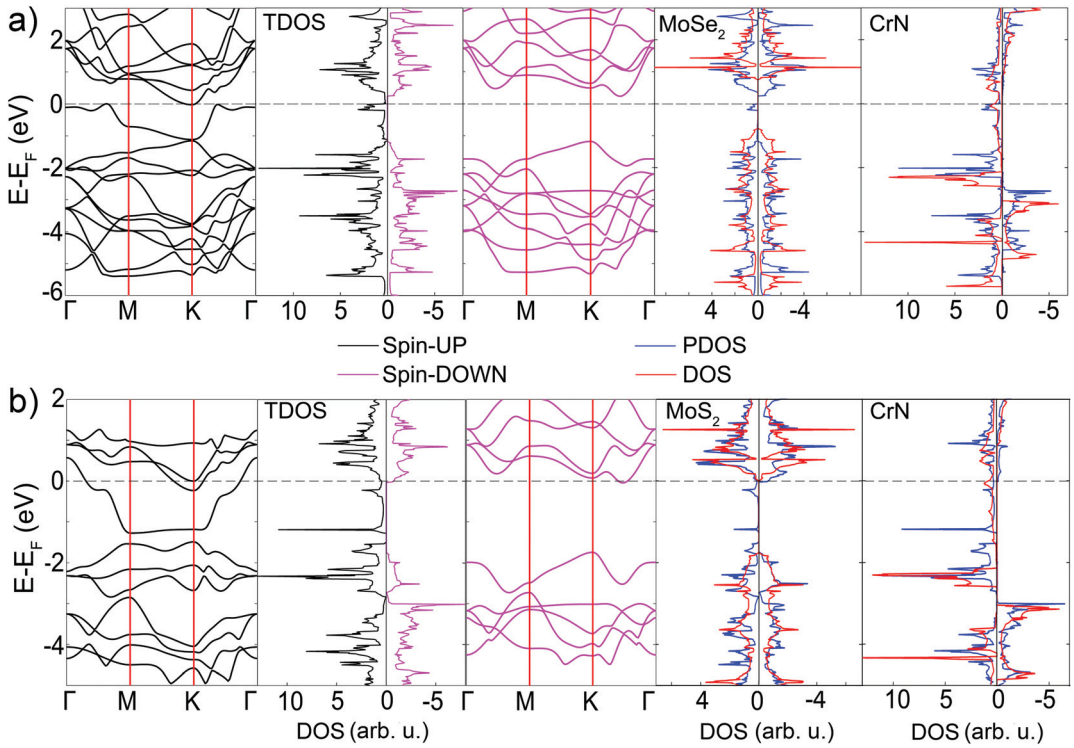

Fig. 5 Band structures (spin-up and spin-down are black and pink, respectively) and densities of states of (a) Cr_[Se]–N_[Mo] and (b) Cr_[S]–N_[Mo] configurations. DOSes of freestanding $MoSe_2$, MoS_2 and *h*-CrN sheets are presented in red and corresponding PDOSes are plotted in blue. Spin-up and spin-down DOS channels are demonstrated from left to right.

small-intensity peaks near the Fermi level in the spin-up channel, whereas PDOSes of *h*-CrN are decreased at the Fermi level and shifted to the higher energy interval (Fig. 5(a)). The band structures at the top of the valence band and bottom of the conductivity band of Cr_[Se]–N_[Mo] and Cr_[Se]–N_[hex] configurations are changed with decreasing the density of states at the Fermi level, however, the main features of *h*-CrN are retained. All configurations are 100% spin polarized with a 1.43 eV spin-down band gap of the lowest-energy Cr_[Se]–N_[Mo] configuration. The third in energy configuration (Fig. S5†) demonstrates the higher spin-up density of states at the Fermi level among all three *h*-CrN/$MoSe_2$ configurations. It can be concluded that the difference (in energy and electronic structure) in the final location of a nitrogen atom ([Mo] or [hex]) is negligible due to the similar distance and electrostatic interaction between the nitrogen and nearest substrate Se atoms. The minor difference between [Mo] and [hex] nitrogen configurations rises from the distance and interaction with the second substrate layer (Mo). All three *h*-CrN/$MoSe_2$ configurations are similar in electronic structure and may be of interest for spin-related applications.

The band structures and partial densities of state of the lowest in energy Cr_[S]–N_[Mo] and two other configurations of *h*-CrN/MoS_2 are presented in Fig. 5(b) and S6,† respectively. The first two configurations clearly demonstrate the 100% spin-polarized half-metallic nature of *h*-CrN and MoS_2 fragments with 1.71 eV spin-down band gaps, whereas Cr_[hex]–N_[Mo] exhibits a magnetic semiconducting nature with a narrow indirect band gap (0.17 eV) in the spin-up state and direct band gap (1.79 eV) in the spin-down state. The interactions between the fragments lead to a significant increase of the densities of state at the Fermi level in comparison with freestanding *h*-CrN (Fig. 2(e)), and convert MoS_2 to the half-metallic state.

The Bader analysis of electronic density distribution reveals small and almost identical charge transfers of 0.07 and 0.08 electrons from *h*-CrN to the $MoSe_2$ sheet for two energetically preferable configurations ([Mo] and [hex] nitrogen positions), respectively. The total charge transfers from *h*-CrN to the MoS_2 monolayer for the [Mo] and [hex] nitrogen positions are 0.19*e* and 0.18*e*, which may be caused by stronger bonding between *h*-CrN and MoS_2 in comparison with the *h*-CrN/$MoSe_2$ composite. The higher charge transfer and lower cohesive energy are primarily caused by the higher sulfur electronegativity in comparison with selenium and the small atomic radius resulting in relatively shorter interlayer distances between MoS_2 and *h*-CrN. The magnetic moments localized on the Cr (2.85–2.86μ_B) and Mo (0.10–0.11μ_B) ions were detected as well. The first selenium ion, which is directly bonded with Cr, has 0.027μ_B, whereas an almost zero magnetic moment (0.005–0.007μ_B for different configurations) was detected for the second Se ion, which is only bound to Mo. The Bader analysis also revealed the 2.74μ_B and 2.77μ_B magnetic moments of Cr^{2+} ions and 0.15μ_B and 0.18μ_B for Mo ions in the Cr_[S]–N_[Mo]

Open Access Article. Published on 24 November 2016. Downloaded on 7/24/2025 7:54:59 PM.
This article is licensed under a Creative Commons Attribution-NonCommercial 3.0 Unported Licence.

and Cr_[S]–N_[hex] configurations, respectively. The sulfur ions have 0.027–0.035μ_B in positions directly bound to Cr and 0.015–0.017μ_B in positions which are only bound to Mo ions, respectively. In general, the visible reduction of Cr magnetic moments in *h*-CrN/$MoSe_2$ and *h*-CrN/MoS_2 heterostructures is caused by redistribution of the charge during the formation of weak bonds with the substrate and therefore reduction of number of unpaired electrons in the system.

The shapes of all TDOSes do not appear as a superposition of particular components (dichalcogenides and *h*-CrN) revealing the interaction between the monolayers. The most obvious resonance peaks are in the [−0.19: 0] eV energy interval for $MoSe_2$ and the [−0.31: −0.21], [−1.21: −1.15], [−1.73: −1.68] eV energy intervals for MoS_2. To understand the nature of the interaction between the monolayers, the spatial charge density distributions were analyzed (Fig. S7†). The peak at the Fermi level exhibits a non-binding electronic state. The formation of the *h*-CrN/$MoSe_2$ composite shifts the peak to the lower energy level. This fact demonstrates weak bonding between $MoSe_2$ and *h*-CrN which can be proved by the overlap in charge density distribution as well as by DOS resonance in the [−0.19: 0] eV energy interval. Partial peaks of the Cr and S states are localized in the same energy range of [−1.21: −1.15] eV and demonstrate the exact same electronic resonance, revealing a strong overlap between them. The other peaks show a more complex interaction character revealing the appearance of electron density at the Mo atoms, which can be explained as a polarization effect of the composite. It can be concluded that the interaction between the fragments leads to the orbital overlap due to the coincident peaks of *h*-CrN and $MoSe_2$ or MoS_2 at the Fermi level. The joint effect of electrostatic forces and orbital overlapping results in the formation of bonds between monolayers. These results indicate that the choice of a correct substrate can play a crucial role in *h*-CrN synthesis. In this way, both $MoSe_2$ and MoS_2 substrates keep the half-metallic properties of 2D *h*-CrN. The difference generally lies in the amplitude of the densities of state at the Fermi level. The $MoSe_2$ substrate has a low electron density at the Fermi level whereas MoS_2 has much higher one. It is apparent that the different S and Se electronegativity caused by the different charge transfers leads to electron density redistribution, altering the final properties of the composites.

To investigate the optical properties of *h*-CrN -based nanocomposites, the frequency-dependent dielectric matrix was calculated and refractive indexes (n) and extinction coefficients (k) were determined as:

$$n = \sqrt{\frac{\sqrt{(\varepsilon')^2 + (\varepsilon'')^2} + \varepsilon'}{2}}, \quad (4)$$

$$k = \sqrt{\frac{\sqrt{(\varepsilon')^2 + (\varepsilon'')^2} - \varepsilon'}{2}}, \quad (5)$$

where ε' and ε'' are the real and imaginary parts of the complex dielectric function.

The refractive indexes and extinction coefficients of freestanding *h*-CrN, *h*-CrN/$MoSe_2$ and *h*-CrN/MoS_2 composites, calculated for perpendicular light polarization are presented in Fig. 6. The intensities of *h*-CrN absorption and refractive spectra rapidly increase from the ultraviolet (UV) to the infrared (IR) spectral regions with a maximum in the IR region. In the UV and visible light regions one-atom-thick *h*-CrN exhibits high transparency and enhanced light refraction compared with graphene.[75] The high transparency of *h*-CrN is caused by the low probabilities of averaged electronic transitions with appropriate transition energies between the valence and conduction bands.

The extinction coefficients of both *h*-CrN/$MoSe_2$ and *h*-CrN/MoS_2 composites become lower than those of *h*-CrN in the UV and visible regions. The increase of transparency of the heterostructures in comparison with freestanding *h*-CrN is caused by the decreased probability of averaged electronic transitions in the UV-visible light energy regions caused by the overlap of the electronic states of the *h*-CrN and $MoSe_2$ or MoS_2 fragments.

It is important to note that the synthesis of 2D hexagonal gallium nitride, which is similar in structure to *h*-CrN, was performed very recently *via* a migration-enhanced encapsulated growth (MEEG) technique utilizing epitaxial graphene.[76] This provides new capabilities to further the synthesis of many novel 2D materials that are considered as existing only in the framework of theory for now.

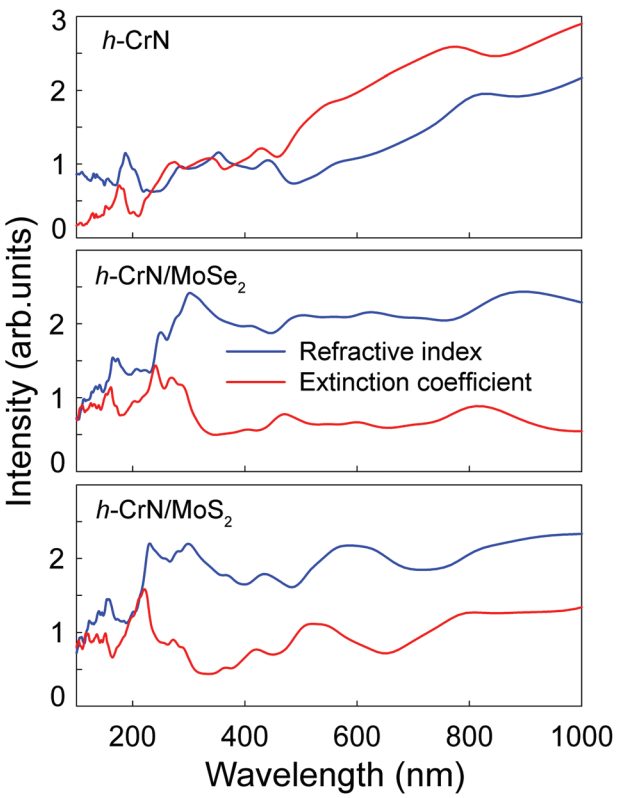

Fig. 6 The refractive indexes *n* (in blue) and extinction coefficients *k* (in red) of freestanding *h*-CrN, *h*-CrN/$MoSe_2$ and *h*-CrN/MoS_2 composites (from top to bottom).

This journal is © The Royal Society of Chemistry 2017

Open Access Article. Published on 24 November 2016. Downloaded on 7/24/2025 7:54:59 PM.
This article is licensed under a Creative Commons Attribution-NonCommercial 3.0 Unported Licence.

Conclusions

In conclusion, a novel one-atom thick two-dimensional hexagonal CrN (*h*-CrN) with unique electronic properties was proposed using DFT+U electronic structure calculations. It was found that *h*-CrN is a 100% polarized half-metal with possible ferromagnetic ordering, which may be optimal for key spin-related applications; therefore no magnetic substrates or doping with atoms would be necessary to induce spin injection to bear spin currents, as in typical 2D materials (*e.g.* graphene, *h*-BN). The crystalline lattice of *h*-CrN has a 1–2.8% mismatch with the lattices of $MoSe_2$ and MoS_2, which can be used as substrates to synthesize *h*-CrN/$MoSe_2$ or *h*-CrN/MoS_2 heterostructures and finally, freestanding *h*-CrN. Both *h*-CrN/$MoSe_2$ and *h*-CrN/MoS_2 heterostructures retain the 100% spin-polarized half-metallic nature of *h*-CrN with the reduction of the *h*-CrN spin-down band gap from 3.9 eV to 1.43 eV and 1.71 eV, respectively. Calculations of dielectric functions of *h*-CrN, *h*-CrN/$MoSe_2$ and *h*-CrN/MoS_2 show the high transparency of all three low-dimensional nanomaterials.

Acknowledgements

We acknowledge the Siberian Supercomputer Center (SSCC) of SB RAS, Novosibirsk; the Institute of Computational Modeling of SB RAS, Krasnoyarsk; the Joint Supercomputer Center of RAS, Moscow; and the ICC of Novosibirsk State University for providing the computing resources. This work was supported by the government contract of the Ministry of Education and Science of the Russian Federation to Siberian Federal University (Grant No. 16.1500.2014/K). P. V. A. acknowledges the Kyungpook National University Research Fund, 2014. N. S. M. acknowledges the Russian Foundation for Basic Research (RFBR 16-32-60003 mol_a_dk).

References

1 K. S. Novoselov, D. Jiang, F. Schedin, T. J. Booth, V. V. Khotkevich, S. V. Morozov and A. K. Geim, *Proc. Natl. Acad. Sci. U. S. A.*, 2005, **102**, 10451–10453.
2 S. Stankovich, D. A. Dikin, G. H. B. Dommett, K. M. Kohlhaas, E. J. Zimney, E. A. Stach, R. D. Piner, S. T. Nguyen and R. S. Ruoff, *Nature*, 2006, **442**, 282–286.
3 B. Aufray, A. Kara, S. Vizzini, H. Oughaddou, C. Léandri, B. Ealet and G. Le Lay, *Appl. Phys. Lett.*, 2010, **96**, 183102.
4 B. Lalmi, H. Oughaddou, H. Enriquez, A. Kara, S. Vizzini, B. Ealet and B. Aufray, *Appl. Phys. Lett.*, 2010, **97**, 223109.
5 E. Bianco, S. Butler, S. Jiang, O. D. Restrepo, W. Windl and J. E. Goldberger, *ACS Nano*, 2013, **7**, 4414–4421.
6 H. Liu, A. T. Neal, Z. Zhu, Z. Luo, X. Xu, D. Tománek and P. D. Ye, *ACS Nano*, 2014, **8**, 4033–4041.
7 F. Zhu, W. Chen, Y. Xu, C. Gao, D. Guan, C. Liu, D. Qian, S.-C. Zhang and J. Jia, *Nat. Mater.*, 2015, **14**, 1020–1025.
8 A. J. Mannix, X.-F. Zhou, B. Kiraly, J. D. Wood, D. Alducin, B. D. Myers, X. Liu, B. L. Fisher, U. Santiago, J. R. Guest, M. J. Yacaman, A. Ponce, A. R. Oganov, M. C. Hersam and N. P. Guisinger, *Science*, 2015, **350**, 1513–1516.
9 S. Z. Butler, S. M. Hollen, L. Cao, Y. Cui, J. A. Gupta, H. R. Gutiérrez, T. F. Heinz, S. S. Hong, J. Huang, A. F. Ismach, E. Johnston-Halperin, M. Kuno, V. V. Plashnitsa, R. D. Robinson, R. S. Ruoff, S. Salahuddin, J. Shan, L. Shi, M. G. Spencer, M. Terrones, W. Windl and J. E. Goldberger, *ACS Nano*, 2013, **7**, 2898–2926.
10 J. Haruyama, *Electronics*, 2013, **2**, 368–386.
11 T. Hashimoto, S. Kamikawa, D. Soriano, J. G. Pedersen, S. Roche and J. Haruyama, *Appl. Phys. Lett.*, 2014, **105**, 183111.
12 C. Ohata, R. Tagami, Y. Nakanishi, R. Iwaki, K. Nomura and J. Haruyama, *Appl. Phys. Lett.*, 2016, **109**, 133110.
13 Y. Nakanishi, A. Ishi, C. Ohata, D. Soriano, R. Iwaki, K. Nomura, M. Hasegawa, T. Nakamura, S. Katsumot, S. Roch and J. Haruyama, *Nano Res.*, 2016, DOI: 10.1007/s12274-016-1355-8.
14 E. A. Kovaleva, A. A. Kuzubov, P. V. Avramov, A. V. Kuklin, N. S. Mikhaleva and P. O. Krasnov, *Org. Electron.*, 2016, **37**, 55–60.
15 M. V. Kamalakar, A. Dankert, J. Bergsten, T. Ive and S. P. Dash, *Sci. Rep.*, 2014, **4**, 6146.
16 A. A. Kuzubov, E. A. Kovaleva, P. Avramov, A. V. Kuklin, N. S. Mikhaleva, F. N. Tomilin, S. Sakai, S. Entani, Y. Matsumoto and H. Naramoto, *J. Appl. Phys.*, 2014, **116**, 84309.
17 P. A. Bhobe, A. Chainani, M. Taguchi, T. Takeuchi, R. Eguchi, M. Matsunami, K. Ishizaka, Y. Takata, M. Oura, Y. Senba, H. Ohashi, Y. Nishino, M. Yabashi, K. Tamasaku, T. Ishikawa, K. Takenaka, H. Takagi and S. Shin, *Phys. Rev. Lett.*, 2010, **104**, 236404.
18 L. M. Corliss, N. Elliott and J. M. Hastings, *Phys. Rev.*, 1960, **117**, 929–935.
19 M. S. Miao and W. R. L. Lambrecht, *Phys. Rev. B: Condens. Matter*, 2005, **71**, 214405.
20 J. D. Browne, P. R. Liddell, R. Street and T. Mills, *Phys. Status Solidi A*, 1970, **1**, 715–723.
21 R. M. Ibberson and R. Cywinski, *Physica B: Condens. Matter*, 1992, **180–181**, 329–332.
22 C. R. Eddine, M. N. Sayetat, F. Felix and E. Hebd, *Seances Acad. Sci., Ser. B*, 1969, **269**, 574–577.
23 C. Constantin, M. B. Haider, D. Ingram and A. R. Smith, *Appl. Phys. Lett.*, 2004, **85**, 6371.
24 A. Glaser, S. Surnev, M. G. Ramsey, P. Lazar, J. Redinger, R. Podloucky and F. P. Netzer, *Surf. Sci.*, 2007, **601**, 4817–4823.
25 P. Lazar, B. Rashkova, J. Redinger, R. Podloucky, C. Mitterer, C. Scheu and G. Dehm, *Thin Solid Films*, 2008, **517**, 1177–1181.
26 K. Inumaru, K. Koyama, N. Imo-oka and S. Yamanaka, *Phys. Rev. B: Condens. Matter*, 2007, **75**, 54416.
27 E. Yang, H. Ji, J. Kim, H. Kim and Y. Jung, *Phys. Chem. Chem. Phys.*, 2015, **17**, 5000–5005.

Open Access Article. Published on 24 November 2016. Downloaded on 7/24/2025 7:54:59 PM.
This article is licensed under a Creative Commons Attribution-NonCommercial 3.0 Unported Licence.

28 C. Eames and M. S. Islam, *J. Am. Chem. Soc.*, 2014, **136**, 16270–16276.
29 A. L. Ivanovskii and A. N. Enyashin, *Russ. Chem. Rev.*, 2013, **82**, 735–746.
30 W.-F. Chen, J. T. Muckerman and E. Fujita, *Chem. Commun.*, 2013, **49**, 8896.
31 Z. Zhang, X. Liu, B. I. Yakobson and W. Guo, *J. Am. Chem. Soc.*, 2012, **134**, 19326–19329.
32 R.-Q. Zhang, C.-E. Kim, B. Delley, C. Stampfl and A. Soon, *Phys. Chem. Chem. Phys.*, 2012, **14**, 2462–2467.
33 Y. Bai, K. Deng and E. Kan, *RSC Adv.*, 2015, **5**, 18352–18358.
34 S. Zhang, Y. Li, T. Zhao and Q. Wang, *Sci. Rep.*, 2014, **4**, 5241.
35 M. Khazaei, M. Arai, T. Sasaki, C.-Y. Chung, N. S. Venkataramanan, M. Estili, Y. Sakka and Y. Kawazoe, *Adv. Funct. Mater.*, 2013, **23**, 2185–2192.
36 A. V. Kuklin, A. A. Kuzubov, N. S. Eliseeva, F. N. Tomilin, A. S. Fedorov and P. O. Krasnov, *Phys. Solid State*, 2014, **56**, 229–234.
37 S. Zhao, W. Kang and J. Xue, *Appl. Phys. Lett.*, 2014, **104**, 133106.
38 M. Naguib, O. Mashtalir, J. Carle, V. Presser, J. Lu, L. Hultman, Y. Gogotsi and M. W. Barsoum, *ACS Nano*, 2012, **6**, 1322–1331.
39 M. Naguib, J. Halim, J. Lu, K. M. Cook, L. Hultman, Y. Gogotsi and M. W. Barsoum, *J. Am. Chem. Soc.*, 2013, **135**, 15966–15969.
40 J. Häglund, A. Fernández Guillermet, G. Grimvall and M. Körling, *Phys. Rev. B: Condens. Matter*, 1993, **48**, 11685–11691.
41 P. B. Sorokin, A. G. Kvashnin, Z. Zhu and D. Tománek, *Nano Lett.*, 2014, **14**, 7126–7130.
42 S. Anand, K. Thekkepat and U. V. Waghmare, *Nano Lett.*, 2016, **16**, 126–131.
43 L. Zhou, B. Shao, W. Shi, Y. Sun, C. Felser, B. Yan and T. Frauenheim, *2D Mater.*, 2016, **3**, 35022.
44 W. Kohn and L. J. Sham, *Phys. Rev.*, 1965, **140**, A1133–A1138.
45 P. Hohenberg, *Phys. Rev.*, 1964, **136**, B864–B871.
46 V. I. Anisimov, J. Zaanen and O. K. Andersen, *Phys. Rev. B: Condens. Matter*, 1991, **44**, 943–954.
47 S. L. Dudarev, S. Y. Savrasov, C. J. Humphreys and A. P. Sutton, *Phys. Rev. B: Condens. Matter*, 1998, **57**, 1505–1509.
48 G. Kresse and J. Furthmüller, *Phys. Rev. B: Condens. Matter*, 1996, **54**, 11169–11186.
49 G. Kresse and J. Hafner, *Phys. Rev. B: Condens. Matter*, 1993, **47**, 558–561.
50 P. E. Blöchl, *Phys. Rev. B: Condens. Matter*, 1994, **50**, 17953–17979.
51 J. P. Perdew, K. Burke and M. Ernzerhof, *Phys. Rev. Lett.*, 1996, **77**, 3865–3868.
52 A. Herwadkar and W. R. L. Lambrecht, *Phys. Rev. B: Condens. Matter*, 2009, **79**, 35125.
53 S. Grimme, *J. Comput. Chem.*, 2006, **27**, 1787–1799.
54 J. Heyd, G. E. Scuseria and M. Ernzerhof, *J. Chem. Phys.*, 2003, **118**, 8207.
55 H. J. Monkhorst and J. D. Pack, *Phys. Rev. B: Solid State*, 1976, **13**, 5188–5192.
56 S. Baroni, S. de Gironcoli, A. Dal Corso and P. Giannozzi, *Rev. Mod. Phys.*, 2001, **73**, 515–562.
57 A. Togo and I. Tanaka, *Scr. Mater.*, 2015, **108**, 1–5.
58 E. M. Landau and L. D. Lifshitz, *Quantum Mechanics*, Pergamon, Oxford, U.K., 1981.
59 E. M. Landau and L. D. Lifshitz, *Statistical Physics Part I*, Oxford, U.K., 1980.
60 I. Choudhuri, S. Kumar, A. Mahata, K. S. Rawat and B. Pathak, *Nanoscale*, 2016, **8**, 14117–14126.
61 J. Zhou, J. Huang, B. G. Sumpter, P. R. C. Kent, Y. Xie, H. Terrones and S. C. Smith, *J. Phys. Chem. C*, 2014, **118**, 16236–16245.
62 C. A. Marianetti and H. G. Yevick, *Phys. Rev. Lett.*, 2010, **105**, 245502.
63 A. Živković and I. Lukačević, *J. Alloys Compd.*, 2016, **682**, 839–843.
64 P. Avramov, V. Demin, M. Luo, C. H. Choi, P. B. Sorokin, B. Yakobson and L. Chernozatonskii, *J. Phys. Chem. Lett.*, 2015, **6**, 4525–4531.
65 N. Nakanishi, A. Nagasawa and Y. Murakami, *J. Phys. Colloq.*, 1982, **43**, 4–35.
66 A. B. Mei, O. Hellman, N. Wireklint, C. M. Schlepütz, D. G. Sangiovanni, B. Alling, A. Rockett, L. Hultman, I. Petrov and J. E. Greene, *Phys. Rev. B: Condens. Matter*, 2015, **91**, 54101.
67 E. Sanville, S. D. Kenny, R. Smith and G. Henkelman, *J. Comput. Chem.*, 2007, **28**, 899–908.
68 A. D. Becke and K. E. Edgecombe, *J. Chem. Phys.*, 1990, **92**, 5397.
69 A. Savin, O. Jepsen, J. Flad, O. K. Andersen, H. Preuss and H. G. von Schnering, *Angew. Chem., Int. Ed. Engl.*, 1992, **31**, 187–188.
70 J.-H. Choi, P. Cui, H. Lan and Z. Zhang, *Phys. Rev. Lett.*, 2015, **115**, 66403.
71 V. Tran, R. Soklaski, Y. Liang and L. Yang, *Phys. Rev. B: Condens. Matter*, 2014, **89**, 235319.
72 X. Li, W. Cai, L. Colombo and R. S. Ruoff, *Nano Lett.*, 2009, **9**, 4268–4272.
73 P. Sutter, J. T. Sadowski and E. Sutter, *Phys. Rev. B: Condens. Matter*, 2009, **80**, 245411.
74 F. Bonaccorso, A. Lombardo, T. Hasan, Z. Sun, L. Colombo and A. C. Ferrari, *Mater. Today*, 2012, **15**, 564–589.
75 E. Ochoa-Martínez, M. Gabás, L. Barrutia, A. Pesquera, A. Centeno, S. Palanco, A. Zurutuza and C. Algora, *Nanoscale*, 2015, **7**, 1491–1500.
76 Z. Y. Al Balushi, K. Wang, R. K. Ghosh, R. A. Vilá, S. M. Eichfeld, J. D. Caldwell, X. Qin, Y.-C. Lin, P. A. DeSario, G. Stone, S. Subramanian, D. F. Paul, R. M. Wallace, S. Datta, J. M. Redwing and J. A. Robinson, *Nat. Mater.*, 2016, **15**, 1166–1171.

This journal is © The Royal Society of Chemistry 2017